

Mass transport characterization of platinum group metal-free polymer electrolyte fuel cell electrodes using a differential cell with an integrated electrochemical sensor

Andrew G. Star¹, Guanxiong Wang¹, Samantha Medina^{1,2}, Svitlana Pylypenko^{1,2}, K.C. Neyerlin¹

1. *Chemistry and Nanoscience Center, National Renewable Energy Laboratory, 15013 Denver West Parkway, Golden, Colorado 80401, United States*

2. *Department of Chemistry, Colorado School of Mines, 1500 Illinois St., Golden, Colorado 80401, United States*

Abstract

A method to enable in place measurements of the mass transport resistance for platinum group metal (PGM)-free polymer electrolyte fuel cell electrodes is presented. Thin platinum black layers deposited at the membrane interface served as electrochemical sensors, performing hydrogen oxidation, for hydrogen probe gas molecules while PGM-free catalyst materials, being electro-inactive to hydrogen oxidation, were probed for mass transport resistance through the full layer. Theoretical considerations, assumptions, and future applications of the methodology are discussed. The method is demonstrated on catalyst layers fabricated from a commercially available PGM-free oxygen reduction catalyst. Effective diffusivity measurements using hydrogen were made which were then used to estimate the effective diffusivity of air of the full layer without the confounding effect of electrode flooding. This method complements alternative techniques such as mercury porosimetry or x-ray computed tomography and can be easily adopted by research groups

everywhere to study MEA-level properties of PGM-free catalyst layers and accelerate the development and deployment of PGM-free PEFCs.

Keywords: PGM-free electrocatalyst, PGM-free electrode, electrode transport resistance, hydrogen limiting current

1 INTRODUCTION

Polymer electrolyte fuel cells (PEFC) can replace internal combustion engines, electrify the long-range transportation sector, and avert harmful aerosol pollution in cities, particularly in non-attainment areas. PEFCs with platinum group metal (PGM) catalysts can meet performance targets but still remain too expensive to achieve cost targets and widespread market penetration¹. Alternatively, PGM-free PEFCs can already meet cost targets and may reach performance targets with additional development. For example, a recent report by Banham et al. showed that an Fe-N-C catalyst was able to meet the US Department of Energy specified performance targets for stationary power applications². The fact that the precise nature of the oxygen reduction reaction (ORR) active site in Fe-N-C remains incompletely understood³ suggests that possible improvement in PGM-free devices remains unrealized and that these materials may eventually achieve transportation application performance targets. A vast array of possible catalysts are being considered^{4,5} but pyrolyzed, atomically-dispersed Fe/Co/Mn-N-C materials are believed to be the most promising PGM-free catalysts and research into novel syntheses for tailoring materials and devices at atomic-, micro-, meso-, and macro-scales is currently underway.^{3,6}

Improvements in turn-over frequency and active-site density are necessary for a competitive, high-power density device. Accordingly, PGM-free PEFC research has largely focused on catalyst development assessed via oxygen reduction reaction (ORR) activity in half-cells with less attention paid to electrode development and membrane electrode assembly (MEA) integration. However, ORR activity is necessary but insufficient for a high-performance device and researchers have pointed out that the intrinsically lower volumetric activity of PGM-free catalyst (cf. PGM) obliges increased areal catalyst loading to reduce the kinetic overpotential of the cell.⁷ Unfortunately, increasing catalyst loading concomitantly increases electrode thickness and may reduce electrode porosity. Both of these changes to the electrode layer increase the concentration overpotential of the cell by increasing the effective transport path lengths for oxygen diffusion and proton conduction, assuming full electrode utilization.⁸ Moreover, without precise control of the electrode microstructure during fabrication, inhomogeneities could reduce the areal density of percolating channels for gas transport and water removal. These challenges have been reviewed recently in literature. Martinez et al. discussed the disparity between PGM-free microstructures of RDE-deposited electrodes and MEA-integrated electrodes, emphasizing the need for in situ MEA characterization.⁶ Wu emphasized the need for advanced synthesis routes with greater attention toward choice of precursor molecules that could ultimately result in electrode improvements across all length scales.³ In an exemplary step forward, Chung et al. hybridized polyaniline (PANI) and cyanamide (CM) precursors to generate a hierarchical electrode with high porosity and substantial meso- and macro-pore structure.⁹ Their catalyst performed nearly as well as Pt/C in an H₂-air full cell which they attributed largely to the high porosity and well-connected pore structure of the electrode. Li et al. also ascribed the impressive device-level performance of their MOF-derived catalyst to a large and well-percolating secondary pore structure, including access to micropores which are believed to contain the active sites.¹⁰ Babu et al. used agglomerate modeling and x-ray CT imaging to demonstrate the importance of cathode layer thickness optimization and especially, precise control of the ionomer network via control of catalyst

particle morphology.¹¹ Pavlicek et al. varied the oxygen carrier gas in diffusion experiments to show that limitations of the catalyst layer were the primary source of mass-transfer cell losses.¹²

Consensus has developed within the PGM-free community that successful PGM-free PEFC development must include device-level studies and microstructure optimization, especially for minimizing the concentration overpotential in the thick PGM-free electrode layers. Specifically, the community would benefit greatly from diagnostics capable of deconvoluting specific contributions to mass-transfer resistances such as macro-pore, micro-pore resistance, local resistance very close to the surface of catalytic nanoparticles, and resistance from flooding effects, particularly important for high power density operation. This would be especially useful to complement alternative techniques such as mercury intrusion porosimetry (MIP) or x-ray computed tomography (XCT).^{13,14} MIP cannot measure dead-end pores and may alter the true morphology of PEFC electrodes during measurement due to high capillary pressure required to induce mercury breakthrough/percolation through small pore throat. XCT morphology is obtained at zero electrode hydration and cannot resolve microporosity and some mesoporosity. Toward this end, this report builds upon previous work that has utilized limiting current measurements to characterize operando mass transport resistances in fuel cell materials. Baker et al. and Beuscher first suggested the use of limiting current for mass transport characterization in 2006.^{15,16} The technique has been developed over the past decade for measurement, deconvolution, and quantification of the discrete contributions to the concentration overpotential, often expressed as a mass transport resistance, arising from constituent materials and cell components.^{15,17,18,19,20,21,22} Quantifying these contributions can both benchmark and improve understanding of the physical differences between electrodes fabricated by different methods. In this work, we extend the capability of characterizing mass transport resistances via a new and complementary approach integrating a platinum black (PtB) sensor layer into the membrane electrode assembly (MEA). The PtB sensor platform enables determination of mass transport resistance through the entire electrode thickness in PGM-free catalyst layers using a

transport probe molecule that reacts at the boundary of the porous catalyst layer, not inside of it. This measurement can be thought of as similar to a measurement taken using a Graham cell or a Loschmidt cell.²³ For example, Pant et al. and Mangal et al. performed full-layer mass transport experiments of gas diffusion media using a set up similar to a Graham cell al.^{24,25} Cekmer et al. used a Loschmidt diffusion cell to characterize diffusion media and made significant contributions to the analysis of experimental results.²⁶ Yu and Carter measured in-plane effective diffusivity of humid air in platinum-containing fuel cell electrode layers using a modified dual-channel flow field, somewhat similar to a Loschmidt cell.²⁷ The measurements presented in this work were taken on PGM-free electrode layers that were integrated into MEAs and operated in fuel cell hardware under nearly-realistic cell conditions including realistic cell compression, relative humidity, backpressure, and temperature. To the best of our knowledge, this work reports the first measurements of effective diffusivity of a PGM-free electrode layer.

Section 2 describes the theory and experimental set up, Section 3 describes the workup and validation experiments that were performed, followed by transport characterization of an Fe-N-C electrode layer and relevant discussion. Section 4 offers conclusions from the findings of this work.

2 THEORY AND EXPERIMENTAL DETAILS

2.1 CELL CONFIGURATION

Sensor-integrated cells were fabricated in various “sandwich” assembly arrangements of materials. PGM-free catalyst material layers are referred to as target layers (TL) in this work. The assembly also includes diffusion media (DM), a proton exchange membrane (PEM), a carbon-supported platinum electrode layer as reference electrode (REF), and a thin (ca. 500 nm), PtB sensor layer. In all transport characterization measurements, the PtB layer functioned as the working electrode (WE) while the PGM-free layer was the TL. The WE side of the cell, the TL specifically, was the primary subject of mass transport characterization.

A graphic of the primary assembly used in this report is shown in Figure 1. Flow field channels are unlabeled but are shown on both ends of the assembly as they were compressed within fuel cell hardware.

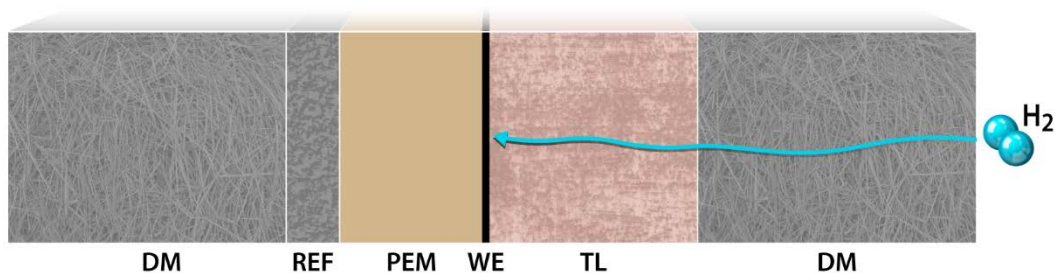


Figure 1 – example of cell assembly fabricated with integrated platinum black sensor and PGM-free target layer.

A crucial distinction from most previous limiting current analysis research was that hydrogen was used as the molecular probe for mass transport resistance instead of oxygen. The use of hydrogen as probe molecule in a PEFC limiting current study appears to have been first reported by Hwang and Weber for investigating gas diffusion media.²⁸ Spingler, et al. later used hydrogen and deuterium in a limiting current study to confirm that CCL platinum loading was inversely related to total transport resistance in the CCL²¹ lending greater support to the platinum-ionomer local mass transport resistance hypothesis.²⁹ In contrast to their study, the PGM-free catalysts used in this work are not electrochemically active to hydrogen at the operating conditions of interest (addressed in section 3.1.1). Accordingly, the TL for transport investigation did not participate in electrochemical reactions which circumvented a fundamental problem of the transport-resistor-in-series model that past work has relied on.¹⁸ In the case of thick catalyst layers, especially true for PGM-free layers, the geometric area-averaged one-dimensional effective path length of gas phase mass transport must be treated as a high variance distribution as compared to a near-constant for very thin layers such as conventional platinum nanoparticles supported on carbon black. The corresponding transport-resistor-in-series model then becomes a transmission-line model but in an arrangement that is unquantifiable without extensive knowledge of the pore network and ionomer distribution in the PGM-free electrode. For example, in a related, foundational analysis, Nonoyama et al.

assumed a uniform reaction distribution in a Pt/C electrode (ca. 10 μm) and an effective electrode thickness of one-third the total thickness corresponding to a uniformly distributed transmission-line model.¹⁹ However, this assumption does not necessarily hold for the thicker layers (ca. 100 μm) used in PGM-free catalysts. Through the approach developed in this paper, the gaseous reactant transport resistance of the entire target layer becomes accessible while relaxing the underlying assumption of reactant distribution. Previous measurements in Graham and Loschmidt cells do not include the effects of realistic compression, humidity, or temperature. This offers a complementary approach for quantifying the transport resistance of full PGM-free catalyst layers. In nearly all experiments, the cell was operated at differential conditions such that the reactant concentration gradient down the channel was negligible.

2.2 MASS TRANSPORT RESISTANCE THEORY

For limiting current tests, 5% H_2 gas (balance N_2) was delivered to both sides of the cell. Applying a positive potential difference across the cell promotes the hydrogen oxidation reaction (HOR) at the WE and the hydrogen evolution reaction (HER) at the REF. The electrochemical half-reactions are given in Equations 1 and 2.



The cell's current density, i_d , is proportional to the flux of hydrogen at the surface of the WE according to Faraday's law.³⁰

$$i_d = nF\mathbf{N}_{\text{H}_2} \quad (3)$$

n is the number of electrons transferred by reaction, F is Faraday's constant, and \mathbf{N}_{H_2} is the molar hydrogen flux. The hydrogen flux in the through-plane direction at steady state and slow scan rates is approximately equal everywhere due to the aspect ratios of cell components, the sandwich construction

of the cell, and differential conditions used. With this condition satisfied, a concentration difference-driven mass transfer process can be assumed between the flow field channel and the surface of the WE.

$$N_{H_2} = \frac{1}{R_{total}} (C_{H_2,channel} - C_{H_2,surf}) \quad (4)$$

$C_{H_2,x}$ is the H₂ concentration at location x in the through-plane and R_{total} is an overall or “total” mass transfer resistance, the reciprocal of mass transfer admittance. When current is drawn until HOR becomes diffusion-limited, the hydrogen concentration at the surface of the WE vanishes. Thus, with uniform hydrogen flux everywhere and uniform down-the-channel concentration, the hydrogen concentration gradient in the through-plane arise from variations in R_{total} . To quantify transport resistances of individual components and processes in the cell, R_{total} can be written as a combination of serial and/or parallel resistances representing each component and/or material in the cell assembly. In this work, the components (TL and DM) were arranged in serial and R_{total} was given by Equation 5.

$$R_{total} = \sum_j R_j \quad (5)$$

Subscript j in Equation 5 denotes the components of the assembly on the cathode side including diffusion media and target material layers. In contrast to studies using oxygen limiting current,²⁰ water and heat generation do not confound the measurement. Combining Equations (3) and (4), R_{total} is written as in Equation 6. All measured crossover and background current densities were small (<10 mA cm⁻²) as compared to the observed limiting current densities (200 – 1000 mA cm⁻²) and were thereby ignored in this work.

$$R_{total} = \frac{nFC_{H_2,channel}}{i_{d,lim}} \quad (6)$$

2.3 MATERIALS AND ELECTRODE FABRICATION

All cells were fabricated using Nafion 211 membranes (DuPont) and 060 carbon paper diffusion media with 5% wet-proofing (Toray). All electrodes were deposited with a Sonotek Exactacoat OP3 in an alternating horizontal and vertical raster pattern. Platinum black (TKK) sensor layers were fabricated from inks of 4:3 ratio deionized water to n-propanol with catalyst mass concentration of $\sim 4 \text{ mg}_{\text{catalyst}} \text{ per mL}_{\text{ink}}$. PtB layer catalyst loadings were $\sim 0.8 \text{ mg}_{\text{Pt}} \text{ cm}^{-2}$ verified by x-ray fluorescence on a Fisher XDV-SDD. The PtB inks excluded ionomer because testing showed no proton transport limitations (see Figure S3). This also avoided the possibility of PtB poisoning via sulfonate side-chain adsorption. REF electrodes were fabricated from inks containing platinum on high surface area carbon (TEC10V50E, TKK) with 5 wt% Nafion ionomer dispersion (DuPont DE2020, Ion Power) at 0.9 ionomer to carbon ratio and 4:3 ratio deionized water to n-propanol. Nominal REF catalyst loadings were $0.2 \text{ mg}_{\text{Pt}} \text{ cm}^{-2}$ also verified by x-ray fluorescence. The PGM-free material used for the TLs was a state-of-the-art commercial Fe-N-C catalyst (PMF-11904, 10 nm pore size, Pajarito Power, LLC). TL inks were 2:1 mixtures of n-propanol to deionized water with catalyst concentration of $\sim 8 \text{ mg per mL}$. The desired mass of ionomer (Dupont DE2020, Ion Power Inc.) was added to obtain either 30 or 45 wt% in the TLs. 7 mil virgin skived PTFE gaskets (Enflo) sealed the active area. The cell was joined by eight bolts spaced by Bellville washers and hand-torqued to 4.5 N m for a nominal DM compression of 20%. 18 M Ω cm deionized water and ultra-high purity gases (Airgas) were used for all experiments.

2.4 SCANNING ELECTRON MICROSCOPY

Cross-sectional and surface images were collected by scanning electron microscopy (SEM). A liquid nitrogen freeze fracture method was used for cross-sectional images. Mean target layer thickness was determined as the mean of more than 10 measurements taken randomly along the length of the cross-sectional images. Thickness values and their standard deviations are reported in Table 2 in the Results

section. All electron micrographs were collected on a JEOL JSM-7000F SEM. An example of a cross-sectional image is shown in Figure 2. The sample imaged in Figure 2 is comprised of, from bottom to top, a Pt/C reference electrode, a proton exchange membrane, a platinum black sensor layer, and an Fe-N-C material layer.

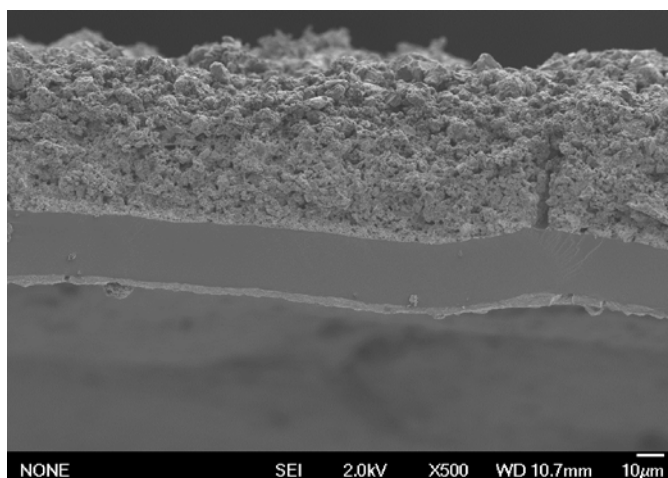


Figure 2 - Example of a cross-sectional image taken for thickness measurement. From bottom to top, the layers are: a REF electrode, a proton exchange membrane, a platinum black sensor layer, and an Fe-N-C material layer.

Fe-N-C layers deposited onto the PtB sensor versus deposited directly onto a PEM were qualitatively assessed, via imaging, for morphological differences. Although a unique interface exists between the Fe-N-C material and PtB which would not exist in an operando cell, there were no differences in bulk morphology observed between target layers deposited onto polymer substrates or PtB substrates.

Because target layers will range from ~40-100 µm, any influence upon the final microstructure of the target layer will likely be confined to the interface between the target layer and the PtB sensor and will not affect the transport of gas through the bulk.

2.5 CELL TESTING

Limiting currents were measured by cyclic voltammetry (CV) with dilute feeds of hydrogen balanced in nitrogen. Three sweeps were collected and the third sweep, undifferentiated from the second sweep, was considered the limiting current value. CVs were collected under both H₂/N₂ and dilute H₂/H₂ environments. A Teledyne Medusa test stand controlled cell temperature, pressure, gas flows, and inlet gas humidity and a Metrohm Autolab 302N potentiostat/galvanostat was used for collecting all electrochemical data. Specialized flow fields were used in order to create differential conditions for the limiting current measurement. Dimensions and images of the flow fields are provided in previous work.¹⁸

3 RESULTS & DISCUSSION

3.1 VALIDATION OF PLATINUM BLACK SENSOR PLATFORM

To ensure consistent limiting current measurements and correct ascription of transport resistances to the target material layers, the platinum black sensor must produce a well-defined limiting current measurement and remain stable and predictable over the course of testing. The PtB sensors used in this work were similar to electrode layers used in prior-generation phosphoric acid fuel cells and PEFCs, before the widespread adoption of carbon supported platinum electrodes. PEFC research activities spanning the 1980's and 1990's demonstrated robust PtB electrodes during typical operation.^{31,32} Benchmarks for the time frame and operational conditions for sensor stability can be drawn from durability experiments in these systems. For example, Ralph et al. demonstrated that platinum black electrodes (anode and cathode) were stable under ORR operation in MEAs over hundreds of hours of steady-state operation.^{33,34} More recently, Chen et al. performed a common accelerated stress test on a platinum black (E-TEK) electrode in half-cell configuration and showed no change in ECSA after 50 cycles and <5% ECSA loss after 100 cycles.³⁵ In studies using hydrogen reformed from methane, trace organics and CO can poison the

platinum however, use of ultra-high purity gases for the sensor experiments in this work ensured negligible catalyst poisoning and contamination error from the reactant streams.

3.1.1 Electrochemical Stability

PtB layer electrochemical (HOR) stability was validated to ensure that limiting current measured in sensor- and-PGM-free layer-integrated cells were not caused by sensor-degradation related artifact. A cell was built with a PtB layer and one DM. A diagnostic test was applied to this cell before and after the battery of experiments taken to collect mass transport resistance properties. The diagnostic test was an anodic linear sweep voltammogram at varying scan rate from 0.05 V up to 0.8 V taken at the following cell conditions: $T_{\text{cell}} = 80\text{ }^{\circ}\text{C}$, 85 RH, 600 sccm 5% H_2 at the REF, and 600 sccm 5% H_2 at the WE. Due to the low H_2 percentage used and modest flowrates used, the cell was not operated under differential condition for these experiments whereas limiting currents in subsequent sections were measured under differential conditions. To more easily visualize the limiting current densities and extract accurate values, a power function of the form $\beta_1 x^{\beta_2} + \beta_3$, where β_i were optimal parameters, was fit to the raw data by a trust-region-reflective algorithm. In Figure 3, raw data points are plotted in muted color and the best-fit lines are plotted in bold color to highlight the limiting current.

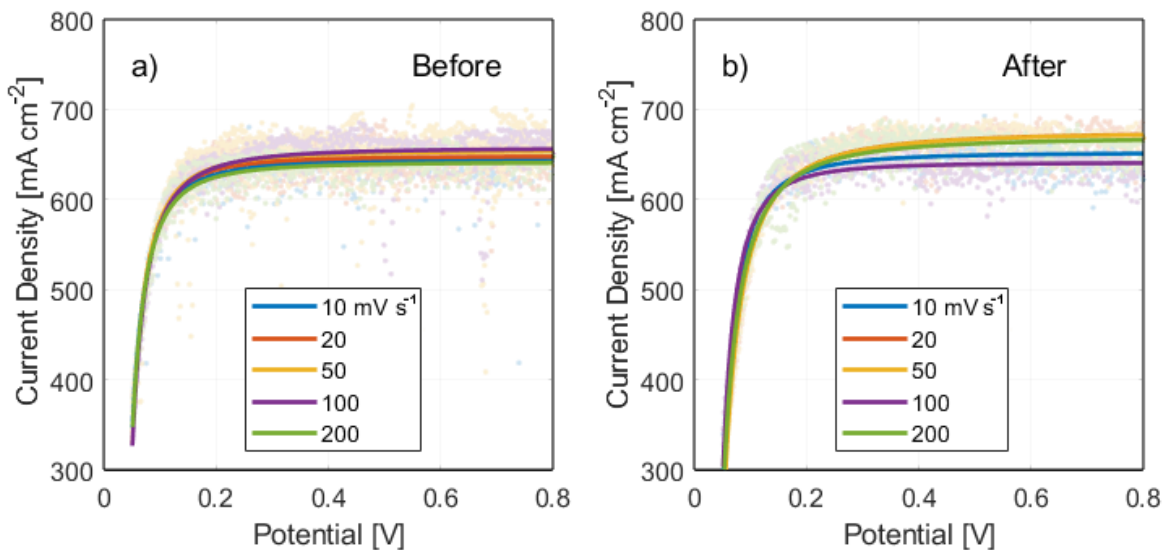


Figure 3 – Diagnostic limiting current response of the platinum black working electrode in a sensor-only cell a) before and b) after experimentation at various scan rates. cell conditions: $T_{cell} = 80\text{ }^{\circ}\text{C}$, 85 RH, $P_{cell} = 150\text{ kPa}$, 600 sccm 5% H_2 at the REF, and 600 sccm 5% H_2 at the WE.

The limiting current density response was slightly noisier after testing but was overall negligibly altered from its initial value after the battery of experiments. This demonstrated the sensor's HOR stability after a representative set of tests as would be experienced by a cell during mass transport resistance testing.

3.1.2 Platform Reproducibility and Non-TL Resistances

To further validate the behavior of the PtB platform, determine the range of feasible operating conditions, and quantify non-TL resistances, a cell with a PtB sensor layer and DM but no target layer was assembled and tested. The cell was again operated at $80\text{ }^{\circ}\text{C}$ but flow rates were increased to 2000 sccm and 5000 sccm at the CE and WE, respectively, in order to ensure differential cell conditions. CVs were scanned at 40 mV s^{-1} and collected three RH values (100, 90, and 75% RH) and four cell pressures for each RH condition (150, 200, 250, and 300 kPa). The limiting current density was reached at $\sim 0.6\text{ V}$ in all cases. A 50% RH condition was also tested but a mass-transport limited current density was not achieved even as the voltage was scanned as high as 0.8 V. Ohmic behavior was still observed at this potential which was

likely due to the inadequate humidity of the membrane and higher reactant channel concentration at the low RH value. Indeed, membrane resistance increased from $\sim 80 \text{ m}\Omega \text{ cm}^2$ to $\sim 160 \text{ m}\Omega \text{ cm}^2$ when decreasing from 75 RH to 50% RH (cf. Figure S2). Accordingly, limiting current density measurements were not considered below 75% RH. In Figure 4, raw data points are again plotted in muted color and the best-fit lines are plotted in bold color to highlight the limiting current density values.

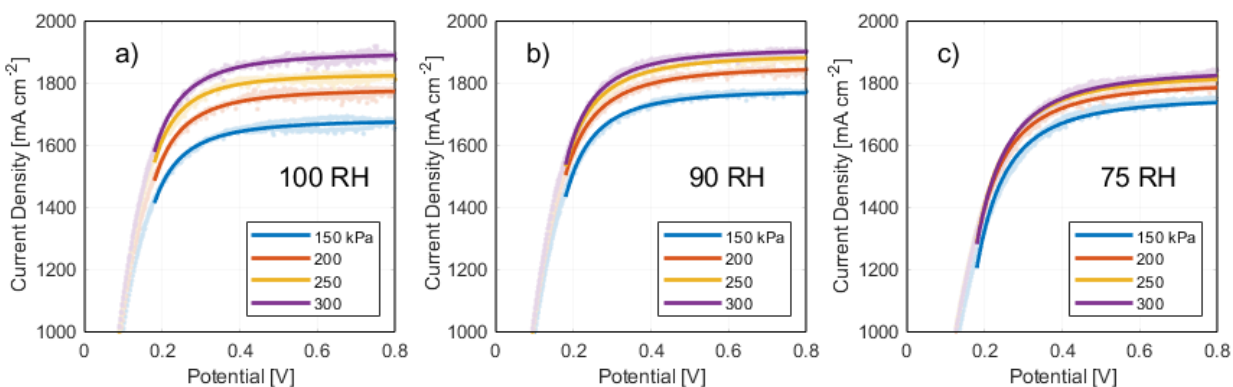


Figure 4 - Limiting current measurements for a standalone PtB sensor under a) 100 RH, b) 90 RH, and c) 75 RH. Limiting current density was collected at four cell pressures for each of three RH values. Raw data is shown in muted color with best-fit lines shown in bold to more easily visualize and aid in accurate extraction of the limiting current density value. $T_{cell} = 80 \text{ }^\circ\text{C}$, 2000 sccm 5% H_2 at the REF, and 5000 sccm 5% H_2 at the WE.

At each RH value, $i_{d,lim}$ scaled directly with pressure because reactant concentration in the channel scaled directly with pressure. The difference between $i_{d,lim}$ at 150 versus 300 kPa increased as RH increased. At high humidity, more of the total gas mixture was occupied by water vapor which resulted in a larger percent change of the reactant concentration at high vs. low humidity as pressure was increased. Specifically, at 100 RH, $C_{\text{H}_2,channel}$ increases by $\sim 250\%$ (1.75 mol m^{-3} to 4.3 mol m^{-3}) when increasing pressure from 150 to 300 kPa. In comparison, at 75 RH, $C_{\text{H}_2,channel}$ increases by $\sim 230\%$ (1.95 mol m^{-3} to 4.5 mol m^{-3}). In contrast, the differences in limiting current observed as RH varied but pressure was held constant were small because $C_{\text{H}_2,channel}$ decreased by only 5-10% when increasing RH from 75 to 100 RH. $i_{d,lim}$ increased slightly with increasing RH which demonstrated that protonic resistance was small but

nontrivial at the high current densities drawn without the presence of a target layer. The effect of porosity reduction due to increased liquid saturation as RH increases was not specifically investigated although it was assumed to be a small effect at the operating conditions used in this work, specifically as water was never generated by electrochemical reaction.³⁶

The total transport resistances of ten PtB sensors from three separate catalyst inks were measured at three different RH values and four pressures. The measured currents, $\sim 2 \text{ A cm}^{-2}$ times 5 cm^2 active area, were too large to ensure negligible concentration gradient down the channel according to stoichiometry, $S = n_{H_2,in}F/i_dA$. Differential conditions assume $C_{inlet} - C_{outlet} \rightarrow 0$ which are likely not met at these conditions, i.e., for $S \approx 4$. This introduces error into the transport resistance analysis for the sensor only experiments, a problem that does not arise for measurements with target layers (shown later in Section 3.1.4). To correct for the gradient in channel concentration for cells without a target layer, a log-mean concentration profile was assumed between the inlet and outlet and a corrected average hydrogen concentration in the channel was written for the high currents drawn. The correction is written in Equation 7 and a derivation is provided in the Electronic Supporting Information (ESI).

$$C_{H_2,AVG} = C_{H_2,in} \frac{\left(\frac{\dot{n}_{H_2,con}}{\dot{n}_{H_2,in}} \right)}{\ln \left(\frac{\dot{n}_{H_2,in}}{\dot{n}_{H_2,in} - \dot{n}_{H_2,con}} \right)} \quad (7)$$

The inlet molar flow of hydrogen, $\dot{n}_{H_2,in}$, was specified by choice of mass flow rate, reactant gas percentage, and process parameters. The consumption rate of hydrogen was determined by $\dot{n}_{H_2,con} = i_dA/nF$ with electron equivalent number, $n = 2$ and active area, $A = 5 \text{ cm}^2$. The corrected transport resistances are plotted in Figure 5. As first demonstrated by Baker et al.,¹⁵ pressure variation at a given RH was used to decouple the pressure-dependent and pressure-independent components of the total transport resistance.

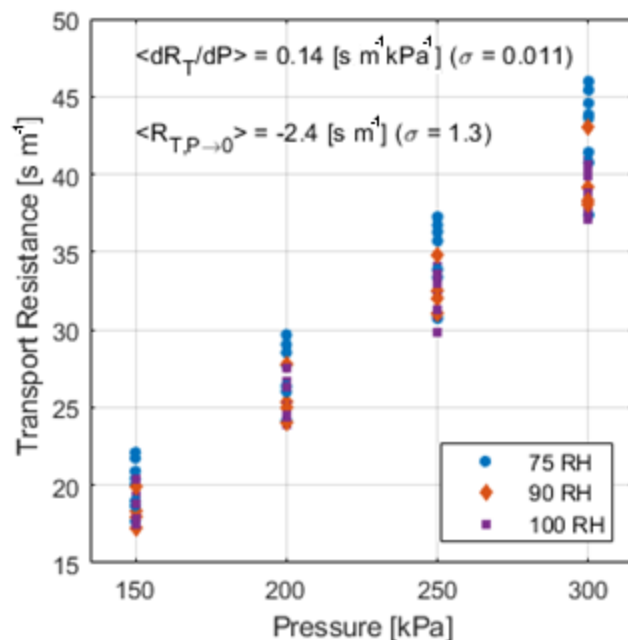


Figure 5 – Corrected total transport resistances for the PtB|DM assembly.

Each trial was fit by linear regression and the mean slope, $\langle \partial R_T / \partial P \rangle$, of all samples was $0.14 \text{ s m}^{-1} \text{ kPa}^{-1}$ with standard deviation, $\sigma = 0.011$. The mean pressure-independent component (the ordinate intercept), $\langle R_{T,P \rightarrow 0} \rangle$, of all samples was $-2.4 \text{ [s m}^{-1}]$ with $\sigma = 1.3$. The ten trials displayed highly reproducible behavior and anticipated limiting behavior of $R_T \rightarrow 0$ as $P_{cell} \rightarrow 0$. The approximately zero intercept demonstrated that both the platinum sensors and the diffusion media exhibited no pressure-independent transport resistances and one highly reproducible pressure-dependent resistance from gas-phase transport in the molecular regime (large pore diameter) DM. The DM resistance measured in this work was in excellent agreement with Nonoyama et al. who determined R_{DM} of 20 s m^{-1} at $80 \text{ }^\circ\text{C}$, 150 kPa , and similar RH.¹⁹ Estimates of systematic and random error in the PtB platform also arose from the ten trials; one may assume approximately -4 s m^{-1} of systematic error due to the negative mean intercept value of -2.4 s m^{-1} (intercept plus one standard deviation). This was likely due to slight inaccuracy in the reactant channel concentration correction. Random error of the platform measurements was estimated

as $\sim 5 \text{ s m}^{-1}$ from the range of values obtained at a given RH among different trials. The mean slopes and intercepts of the plot in Figure 5 are shown in Table 1.

Table 1 – Mean slope and intercept for each of the three RH values.

Property	75 RH	90 RH	100 RH
$\langle \partial R_T / \partial P \rangle$	0.152 ($\sigma = 0.011$)	0.142 ($\sigma = 0.008$)	0.136 ($\sigma = 0.006$)
$\langle R_{T,P \rightarrow 0} \rangle$	-2.72 ($\sigma = 1.46$)	-2.86 ($\sigma = 0.62$)	-1.83 ($\sigma = 1.19$)

Only slight differences in resistance were observed at different RH values. The pressure-independent component of the total transport resistance appeared to increase overall as RH increased but the effect was within error. Increasing RH increases liquid water saturation, reducing porosity and increasing gas-phase mass transport resistance. However, studies of $\text{H}_2|\text{O}_2$ cells with similar diffusion media and RH but at very low or zero current density (such that no water was generated via ORR to contribute to the liquid water saturation) showed very small (ca. 0.01) saturation values consistent with the present study wherein HOR did not generate water.^{37,38}

3.1.3 Target Layer HOR Inactivity

To ensure the PGM-free material used was HOR inactive, a cell was fabricated with a Fe-N-C WE at 2.0 mg cm^{-2} and *without* a PtB. 5% H_2 was delivered to both sides of the cell and a voltammogram was collected (data shown in Figure S1). No oxidation signal was observed during the anodic sweep in the 0.05 – 0.8 V potential window across a range of relative humidity (RH) values and cell pressures demonstrating that the Fe-N-C material used was HOR inactive at the conditions of interest for the limiting current

measurements. This ensured that subsequent measurements in cells with PtB *and* TL could ascribe all Faradaic current to the PtB, not the TL, an essential requirement for Equation 6 to remain valid.

3.1.4 Target Layer Thickness

The mass transport resistance of an electrode is extensive; if electrode layer thickness doubles with all else equal, mass transport resistance will double. Engineering optimal electrode thickness is paramount to PGM-free electrode development due to the low intrinsic ORR activity and necessary high areal catalyst loadings as discussed in the introduction. To address this, high-resolution images were taken to quantify TL thicknesses and to ensure thicknesses were unchanged before and after testing

Table 2 – Measured electrode thicknesses with standard deviations in parentheses.

No.	Thickness	Ionomer Weight %	Before / After	Measured Thickness [μm]
1	Moderate	30%	Before	48 ($\sigma = 5$)
2	Moderate	30%	After	47 ($\sigma = 6$)
3	Moderate	45%	After	46 ($\sigma = 5$)
4	High	30%	After	91 ($\sigma = 4$)

Comparing electrodes #1 and #2 verified that electrode thickness was not appreciably altered due to the mass transport resistance testing applied. This is consistent with stability tests presented in section 3.1.2 Platform Stability. Surface images of the PtB layer (not shown) were also taken to ensure morphology of both the PtB and TLs were not appreciably altered over the duration of testing although slight indentations were observed where diffusion media fibers made contact with the target layer. Cross-sectional imaging further verified that highly uniform PtB layers were deposited with $3 \pm 1 \mu\text{m}$ thickness.

3.2 MASS TRANSPORT RESISTANCE CHARACTERIZATION OF PGM-FREE LAYERS

The PtB sensor platform was shown to be valid and robust. The platform method was applied to three target layers to assess variation across two critical variables in electrode development: ionomer weight percentage and electrode thickness. These correspond to electrode numbers 2, 3, and 4 from Section 3.1.4. Due to the need for high oxygen turnover frequency in operando cells, large areal catalyst loadings, i.e., high thicknesses as described in the introduction, may be required. High ionomer weight percentages may also be required in order to provide a high areal density of percolating ionomer pathways for facile proton conduction and sufficient hydrophobicity for water removal. The full-layer, total transport resistances are plotted for all three target layers as functions of pressure and RH in Figure 6a. In order to isolate the transport resistance of the target layer alone, the transport resistances minus the average resistances of the PtB|DM platform at each pressure and RH condition (taken from Figure 5) are plotted in Figure 6b.

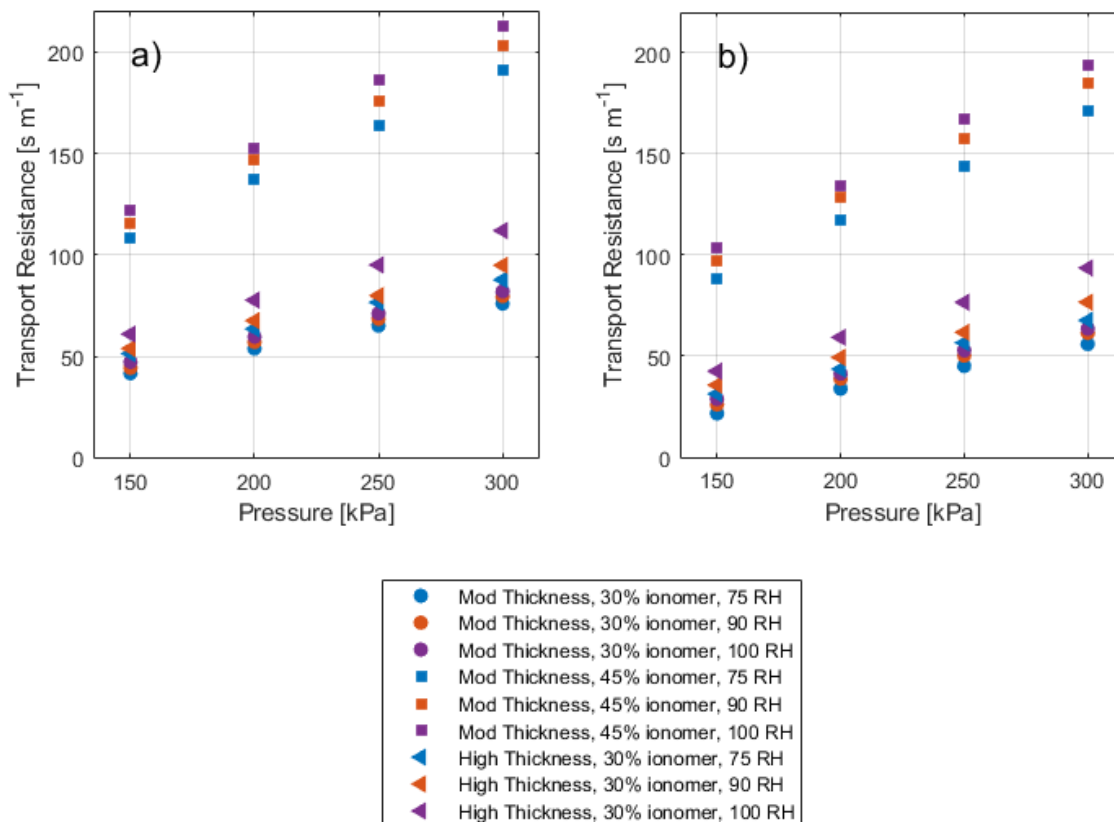


Figure 6 – a) total transport resistance of three target layers with diffusion media at varying RH and pressure and b) total transport resistance of three target layers without diffusion media at varying RH and pressure

Full-layer transport resistance increased significantly when doubling the TL thickness at constant ionomer wt% but increased considerably more when increasing ionomer wt% from 30% to 45% at constant thickness. The observed full-layer resistances qualitatively agreed with results from Yin et al. and Banham et al. who reported considerable improvements in high-current density performance when decreasing ionomer content from 55% to 25% (Yin et al.) and 40% to 35% (Banham et al.).^{39,2} Moreover, a detailed sensitivity analysis by Babu et al. showed that the ionomer behavior had a much larger effect on performance in the mass-transport regime than electrode thickness, just as was observed in the present results.¹¹ Increasing the ionomer content from 30% to 45% at constant thickness increased the full-layer, gas-phase mass transport resistance by a factor of 3-4 at all conditions. It is important to note that this resistance does not include resistance that would arise in an operando cell from mass transfer specifically

toward catalytic sites that are likely embedded in micropores.⁴⁰ Doubling the electrode thickness with equal ionomer content increased the transport resistance by ~50% but did not double as electrode thickness layer doubled.

To better understand these results, note that resistance from macropores scales with pressure and manifests via the resistance-pressure relationship, i.e., the slope, $\partial R_T/\partial P$, of the plot in Figure 6b) while resistance through micropores does not scale with pressure and manifests via the intercept, $R_{T,P \rightarrow 0}$.⁴¹ The slopes and intercepts of the results from Figure 6b) were plotted in Figure 7.

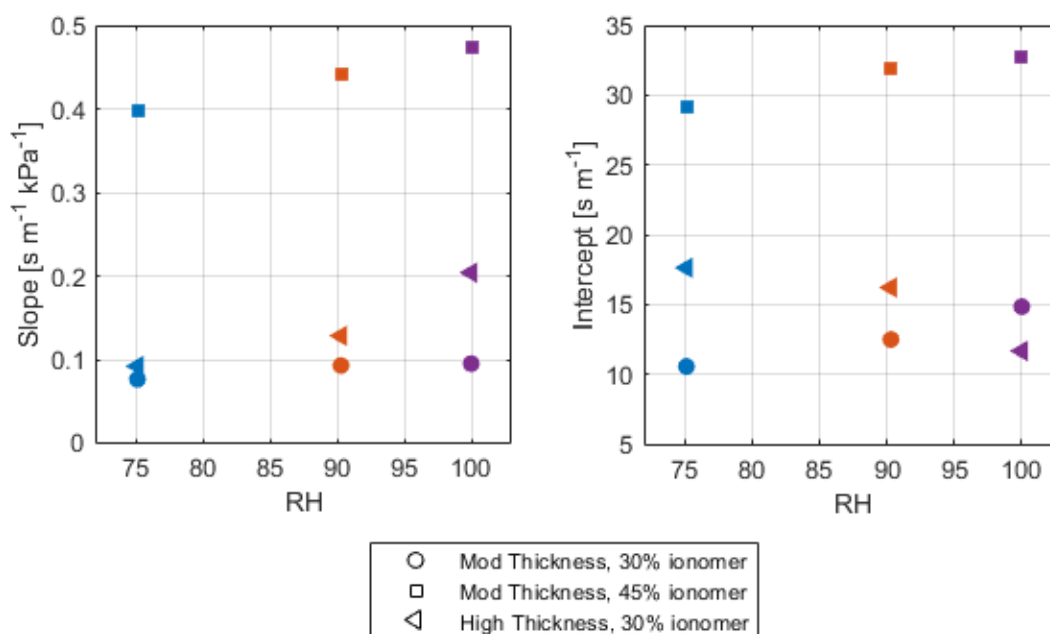


Figure 7 - Slopes and Intercepts from Figure 6b

The comparative trends in slope and intercept for each target layer electrode are described in Table 3.

Table 3 - Comparative trends in slope and intercept as RH was varied for the three electrodes.

No.	Symbol	Thickness	Ionomer Weight %	Pressure-Dependent Resistance ($\partial R_T/\partial P$)	Pressure-Independent Resistance ($R_{T,P \rightarrow 0}$)

2	•	Moderate	30%	low, constant	low, slightly increasing
3	■	Moderate	45%	high, slightly increasing	high, slightly increasing
4	◀	High	30%	low, increasing at high RH	moderate, decreasing at high RH

Increasing ionomer wt% from 30% to 45% (#2 → #3) led to a significant increase in both the intercept and the slope. Taken together, this implies that gas flux through both macropores and micropores were hindered by the increase of ionomer wt%. This was likely due to reduced target layer porosity as incorporation of additional ionomer is well-known to fill voids in porous electrodes as opposed to increasing electrode volume.⁴² A reduced macropore volume and reduced micropore volume would be consistent with the transport resistance results and known behavior of ionomer in porous electrodes. RH had a small effect on the individual electrodes and no significant relative effect between the two electrodes. As a principle for future electrode design, this may rule out ionomer swelling at high RH as an important factor in full-layer gas transport.⁴³ However, ionomer swelling may still be an important consideration for other phenomena that were not probed by the integrated sensor measurements in this work such as reactant adsorption on the electrocatalyst.

Increasing TL thickness from moderate to high thickness (#2 → #4), resulted in nearly double the intercept value and nearly equivalent slopes at sub-saturated humidity (<95 RH). However, as RH approached 100% RH, doubling TL thickness introduced an RH dependence in slope and inverted the scaling relationship of the intercept from direct to inverse proportionality. To help explain this, note that the pore size distribution (PSD) of the same Pajarito material prepared by a nearly identical method (spray coated with a Sono-Tek Exacta-Coat) was assessed in reports by Leonard et al. and Serov et al.^{44,45} In both cases, a nearly bi-modal pore radius distribution was determined for catalyst with ionomer exhibiting a narrow

peak at ~5 nm and a broad peak with maximum at ~100 nm. The broad peak was described as secondary porosity, pores between catalyst aggregates, while the narrow peak was described as primary porosity, i.e., intra-aggregate porosity. Consideration of the relevant transport regimes in the present system requires the mean free path of a dilute gas in a binary mixture. This is given by Equation (8) where n_{H_2} is the number density of hydrogen molecules, σ is the collisional cross-sectional area, and M_j is the molar mass of species j .⁴⁶

$$\lambda = \frac{1}{n_{H_2} \sigma^2 \pi \sqrt{1 + M_{H_2}/M_{N_2}}} \quad (8)$$

Using Equation (8), the Knudsen numbers, $Kn = \lambda/r$, of dilute (5%) hydrogen in nitrogen at 80 °C and 150 kPa for 5 nm and 100 nm pores, respectively, are $Kn = 11$ and $Kn = 1$. Accordingly, gas phase transport in the present system falls within the transition regime in both the primary and secondary pores. Assuming dependence on both porosity and tortuosity and a Bosanquet law for diffusive transport in the transition regime, the resistance of the TL can also be written as in Equation (9).^{47,48}

$$R_{TL} = \frac{L_{TL}}{D_{TL}^{eff}} = L_{TL} \frac{\tau}{\varepsilon} \left(\frac{1}{D_K} + \frac{1}{D_m} \right) \quad (9)$$

D_{TL}^{eff} is the effective diffusivity of the TL, D_K is the Knudsen diffusivity, D_m is the molecular diffusivity, τ is the tortuosity, and ε is the porosity. Thus, if L_{TL} doubled while R_{TL} increased by only ~50%, D_{TL}^{eff} must have increased by ~33%. For single-variable dependence, i.e. sensitivity analysis, this would correspond to 33% decrease in τ , 33% increase in ε , or a 33% increase in either D_K or D_m (for $D_K \cong D_m$). Given the PSD and transition regime diffusion governing the TLs, the comparison between TLs #2 and #4 suggested that the molecular-type resistance resistance was increased while Knudsen-type resistance was decreased. Taken together, this suggests that the high thickness electrode was more substantially impacted by ionomer swelling whereby larger pore radii were reduced to smaller pore radii as would explain the reduction in micropore resistance concomitant with increase in macropore resistance. This is

consistent with the fact that PFSA ionomer very likely cannot impregnate the 5 nm micropores due to steric limitations.⁴⁹ Instead, ionomer swelling in the secondary pore void space likely reduced moderate pore radii to smaller pore radii. Alternatively, these results could be explained by a hydrophobic catalyst layer. If the pores of the TL were overwhelmingly hydrophobic, large radius pores would preferentially fill with water before small pores.⁵⁰ Indeed, thickness swelling of Nafion thin films have been measured as ~15% at high RH.^{51,43} In contrast, if the pores were overwhelmingly hydrophilic, small pores would preferentially become liquid saturated. However, small, Nafion-free pores will likely be hydrophilic as they will be comprised of Fe-N_x sites and/or edge defects in the carbon matrix, i.e., containing terminal C-H bonds cf. extensive graphitic C-C bonds. The increase in TL thickness would also significantly increase the number of constrictive pore throats throughout the layer. These pore throats could have significantly hindered gas phase transport and would be consistent with the results in Figure 6. Although the exact nature of the trends observed in comparing TLs #2 and #4 were not conclusively resolved in this work, the overarching purpose of the platform was well-demonstrated as a viable platform for aiding in the deconvolution of such effects.

From the measured transport resistances and target layer thicknesses, a form of effective oxygen diffusivity can be estimated. We assume Equation 9 holds and that the obstruction factor, ε/τ , is independent of the probe gas. The strategy is as follows: from R_{TL} and L_{TL} , we extract D_{TL,H_2}^{eff} , the effective diffusivity of hydrogen probe gas in the target layer (see supplementary Table S1). The Knudsen and molecular diffusivities for hydrogen in a hydrogen-nitrogen-water vapor mixture are then estimated to obtain the intrinsic obstruction factor of the target layer. The diffusivities of oxygen in an oxygen-nitrogen-water vapor mixture are then estimated and, in combination with the obstruction factor, used to extract the effective diffusivity of the target layer, $D_{TL,air}^{eff}$, as if it were probed by air (21% O₂ in N₂, dry gas). Mathematically,

$$\frac{\varepsilon}{\tau} = D_{TL,H_2}^{\text{eff}} \left(\frac{1}{D_{Kn,H_2}} + \frac{1}{D_{m,H_2}} \right) = D_{TL,air}^{\text{eff}} \left(\frac{1}{D_{Kn,air}} + \frac{1}{D_{m,air}} \right) \quad (10)$$

The Knudsen diffusivities are given by Equation 11.

$$D_{Kn} = \frac{2\langle r \rangle}{3} \sqrt{\frac{8RT}{\pi M}} \quad (11)$$

$\langle r \rangle$ is the average pore radius of the target layer and M is the molar mass of the probe gas. The binary, molecular diffusivity of gas i in gas j can be determined by the Fuller, Schettler, Giddings correlation, given by Equation 12.^{52,41}

$$D_{H_2,j} = \frac{1 \times 10^{-3} T^{1.75}}{p(v_{H_2}^{1/3} + v_j^{1/3})^2} \sqrt{\left(\frac{1}{M_{H_2}} + \frac{1}{M_j} \right)} \quad (12)$$

v_j were the diffusional volumes, set equal to 6.1, 18.5, and 13.1 for H₂, N₂, and H₂O, respectively.⁴¹ The diffusivity of the probe gas in the three-component mixture was determined by a linear mixture rule.

$$D_{H_2,mix} = \left(\frac{x_{N_2}}{D_{H_2,N_2}} + \frac{x_{H_2O}}{D_{H_2,H_2O}} \right)^{-1} \quad (13)$$

x_j are the mole fractions and $D_{i,j}$ are the binary diffusivities. A possible source of error emerges from choice of average pore radius of the layer, required for estimating Knudsen diffusivities. As discussed by Leonard et al. and Serov et al., the pore size distribution is nearly bi-modal with peaks at 5 nm and 100 nm. However, the ratio of $D_{TL,air}^{\text{eff}}/D_{TL,H_2}^{\text{eff}}$ only varies from 0.355 to 0.335 at 5 nm versus 100 nm, approximately 5% error. This is plotted in Figure 8.

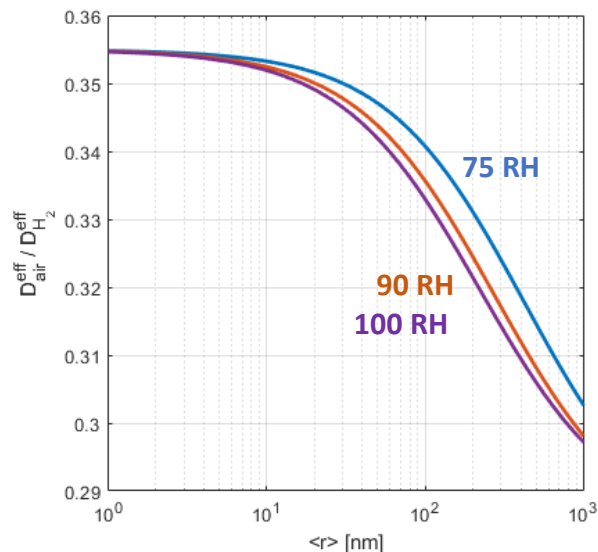


Figure 8 - ratio of effective diffusivities of air to hydrogen probe gas versus average pore radius for 75 RH, 90 RH, and 100 RH.

Interpolating linearly, the ratio $D_{TL,air}^{eff}/D_{TL,H_2}^{eff}$ of 0.345 was used and the estimated effective diffusivities of air in the catalyst layers were tabulated in Table 4.

Table 4 - Estimated air effective diffusivities as calculated from measured hydrogen effective diffusivities.

No.	Symbol	Ionomer Weight %	$D_{TL,air}^{eff}$	$D_{TL,air}^{eff}$	$D_{TL,air}^{eff}$
			75 RH [$\times 10^{-6} \text{ m}^2 \text{ s}^{-1}$]	90 RH [$\times 10^{-6} \text{ m}^2 \text{ s}^{-1}$]	100 RH [$\times 10^{-6} \text{ m}^2 \text{ s}^{-1}$]
2	•	30%	0.75	0.62	0.56
3	■	45%	0.18	0.16	0.15
4	◀	30%	1.00	0.88	0.74

Crucially, $D_{TL,air}^{eff}$ as measured here differs from the effective diffusivity when oxygen is used in an operando cell for two reasons: 1) the measurement in this work probed the full thickness of the target layer, bypassing local transport resistance very close to catalytic reaction sites and 2) because oxygen

reduction (to water) did not take place, the mass-transfer resistance contribution from electrode flooding was avoided. In effect, $D_{TL,air}^{eff}$ is an estimate of the oxygen effective diffusivity of the PGM-free layer minus local transport resistance at the surface of reaction sites and minus resistance due to electrode flooding. Thus, with complementary measurements, this offers the ability to separate out and quantify these local and flooding resistances.

To the best of our knowledge, this was the first in place measurement of effective diffusivity of a PGM-free catalyst layer. The only reasonable comparison available is to Babu et al. who simulated diffusion in silico following nano-XCT imaging of a similar PGM-free layer.⁵³ They used a catalyst material synthesized in house instead of the commercially available catalyst used in this work however, both were Fe-N-C materials. They determined an effective diffusivity of $1.90 \times 10^{-6} \text{ m}^2 \text{ s}^{-1}$ for a 35% ionomer content electrode, about a factor of two larger than what was determined in this work. However, this could be explained by the fact that their catalyst layer morphology was determined/imaged under dry, vacuum conditions and therefore, their simulations were performed on dry catalyst layers. In contrast, the present catalyst layers were hydrated at various, realistic relative humidity values. Taken together, this constitutes possible, early evidence of a ca. 50% reduction in effective reactant diffusivity due to hydration. As a comparison to platinum-carbon fuel cell electrodes, Yu and Carter determined an effective oxygen diffusivity of approximately $6 \times 10^{-7} \text{ m}^2 \text{ s}^{-1}$ in the range of 80-100 RH and 1.0 ionomer to carbon ratio as compared to 0.9 ionomer to carbon ratio in this study. Although their value of effective diffusivity is very close to the value obtained in this work, the possibility for significant morphological distinction between carbon-supported platinum and Fe-N-C layers, and therefore, coincidence in the similarity of obtained values, should not be ignored.

4 CONCLUSIONS

Improved device-level understanding of mass transport limitations in the CCL may help accelerate deployment of low cost, PGM-free PEFCs. Moreover, induction of fundamental structure-mass transport relationships of as-fabricated catalyst layers would be useful to guide ongoing research and development in both catalyst synthesis and membrane electrode assembly fabrication.⁵⁴ This report detailed a complementary method for in place mass transport resistance characterization using an electrochemically-integrated PtB sensor platform that can be easily deployed by research groups everywhere.

Proof-of-concept experiments performed on the three PGM-free target layers demonstrated a significant implication for electrode design. Gas phase mass flux was significantly hindered in the high ionomer content electrode layer, *before* encountering local resistance near catalyst sites. This suggests an important area of opportunity for researchers to address as an operando cell will exhibit an additional transport resistance in serial when reactant transport pathing proceeds toward catalyst sites. Moreover, this method complements other limiting current analyses that do not incorporate a PtB sensor and may help inform related measurements through deconvolution and quantification of individual contributions to mass transport resistance. For example, quantification of full-layer transport resistance in an electrode could be paired with operando resistance measurements to more accurately quantify contributions to electrode voltage losses such as reactant permeation through ionomer thin films and/or closure of pore throats due to ionomer swelling or liquid water saturation and/or compare to advanced techniques such as x-ray nano-CT.^{2,55,56,57} The ability to quantify individual mass-transfer resistance could also be utilized to assess the extent of various degradation modes in durability studies.

Follow up studies in our group are currently underway utilizing this platform to help propose further design principles for electrode fabrication. Furthermore, other groups can adopt this platform, use it for

their own research, and continue to study and extend its capabilities and limitations. This can all help inform researchers how to best proceed with catalyst layer development and rationally learn which designs to rule out.

5 AUTHOR INFORMATION

Corresponding Author

*E-mail: kenneth.neyerlin@nrel.gov

Notes

The authors declare no competing financial interests.

6 ACKNOWLEDGEMENTS

This work was authored in part by Alliance for Sustainable Energy, LLC, the manager and operator of the National Renewable Energy Laboratory for the U.S. Department of Energy (DOE) under Contract No. DE-AC36-08GO28308. Research performed as part of the Electrocatalysis Consortium (ElectroCat), established as part of the Energy Materials Network, which is supported by the U.S. Department of Energy, Office of Energy Efficiency and Renewable Energy, Fuel Cell Technologies Office (FCTO). We acknowledge Ellis Klein, Luigi Osmieri, and Ami Neyerlin for help with experiments; Don Gwinner and Alfred Hicks for help with graphics; and Bryan Pivovar for the useful discussions.

7 REFERENCES

1. Papageorgopoulos, D. *Fuel Cells R&D Overview - 2018 Annual Merit Review and Peer Evaluation*

- Meeting*. (2018). doi:10.1007/s11187-015-9640-6
2. Banham, D. *et al.* Critical advancements in achieving high power and stable nonprecious metal catalyst – based MEAs for real-world proton exchange membrane fuel cell applications. *Sci. Adv.* **4**, 1–7 (2018).
 3. Wu, G. Current challenge and perspective of PGM-free cathode catalysts for PEM fuel cells. *Front. Energy* **11**, 286–298 (2017).
 4. Gewirth, A. A., Varnell, J. A. & Diascro, A. M. Nonprecious Metal Catalysts for Oxygen Reduction in Heterogeneous Aqueous Systems. *Chem. Rev.* **118**, 2313–2339 (2018).
 5. Barkholtz, H. M. & Liu, D.-J. Advancements in rationally designed PGM-free fuel cell catalysts derived from metal–organic frameworks. *Mater. Horiz.* **4**, 20–37 (2017).
 6. Martinez, U., Babu, S. K., Holby, E. F. & Zelenay, P. Durability Challenges and Perspective in the Development of PGM-free Electrocatalysts for the Oxygen Reduction Reaction. *Curr. Opin. Electrochem.* **259**, 293–307 (2018).
 7. Jaouen, F. *et al.* Toward Platinum Group Metal-Free Catalysts for Hydrogen / Air Proton-Exchange Membrane Fuel Cells. 231–255 (2018).
 8. Litster, S. & Mclean, G. PEM fuel cell electrodes. **130**, 61–76 (2004).
 9. Chung, H. T. *et al.* Direct atomic-level insight into the active sites of a high-performance PGM-free ORR catalyst. *Science (80-.)*. **357**, 479–484 (2017).
 10. Li, J. *et al.* Structural and mechanistic basis for the high activity of Fe–N–C catalysts toward oxygen reduction. *Energy Environ. Sci.* **9**, 2418–2432 (2016).
 11. Babu, S. K., Chung, H. T., Zelenay, P. & Litster, S. Modeling Electrochemical Performance of the

- Hierarchical Morphology of Precious Group Metal-Free Cathode for Polymer Electrolyte Fuel Cell. *J. Electrochem. Soc.* **164**, F1037–F1049 (2017).
12. Pavlicek, R. *et al.* Resolving Challenges of Mass Transport in Non Pt-Group Metal Catalysts for Oxygen Reduction in Proton Exchange Membrane Fuel Cells. *J. Electrochem. Soc.* **165**, F589–F596 (2018).
 13. Epting, W. K., Gelb, J. & Litster, S. Resolving the three-dimensional microstructure of polymer electrolyte fuel cell electrodes using nanometer-scale X-ray computed tomography. *Adv. Funct. Mater.* **22**, 555–560 (2012).
 14. Normile, S. J. & Zenyuk, I. V. Imaging ionomer in fuel cell catalyst layers with synchrotron nano transmission x-ray microscopy. *Solid State Ionics* **335**, 38–46 (2019).
 15. Baker, D. R., Wieser, C., Neyerlin, K. C. & Murphy, M. W. The Use of Limiting Current to Determine Transport Resistance in PEM Fuel Cells. *ECS Trans.* **3**, 989–999 (2006).
 16. Beuscher, U. Experimental Method to Determine the Mass Transport Resistance of a Polymer Electrolyte Fuel Cell. *Journal of The Electrochemical Society* **153**, A1788 (2006).
 17. Mashio, T. *et al.* Analysis of Reactant Gas Transport in a Catalyst Layer Tetsuya MASHIO, Atsushi OHMA, Shinji YAMAMOTO, and Kazuhiko SHINOHARA Nissan Research Center, Nissan Motor Co., Ltd., Yokosuka, Kanagawa 237-8523, Japan An analytical. *ECS Trans.* **11**, 529–540 (2007).
 18. Baker, D. R., Caulk, D. A., Neyerlin, K. C. & Murphy, M. W. Measurement of Oxygen Transport Resistance in PEM Fuel Cells by Limiting Current Methods. *J. Electrochem. Soc.* **156**, B991 (2009).
 19. Nonoyama, N., Okazaki, S., Weber, A. Z., Ikogi, Y. & Yoshida, T. Analysis of Oxygen-Transport Diffusion Resistance in Proton-Exchange-Membrane Fuel Cells. *J. Electrochem. Soc.* **158**, B416 (2011).

20. Greszler, T. a., Caulk, D. & Sinha, P. The Impact of Platinum Loading on Oxygen Transport Resistance. *J. Electrochem. Soc.* **159**, F831–F840 (2012).
21. Spingler, F. B., Phillips, A., Schuler, T., Tucker, M. C. & Weber, A. Z. Investigating fuel-cell transport limitations using hydrogen limiting current. *Int. J. Hydrogen Energy* (2017). doi:10.1016/j.ijhydene.2017.01.036
22. Freiberg, A. T. S., Tucker, M. C. & Weber, A. Z. Polarization loss correction derived from hydrogen local-resistance measurement in low Pt-loaded polymer-electrolyte fuel cells. *Electrochem. commun.* (2017). doi:10.1016/j.elecom.2017.04.008
23. Soukup, K., Schneider, P. & Šolcová, O. Comparison of Wicke-Kallenbach and Graham's diffusion cells for obtaining transport characteristics of porous solids. *Chem. Eng. Sci.* **63**, 1003–1011 (2008).
24. Pant, L. M., Mitra, S. K. & Secanell, M. Absolute permeability and Knudsen diffusivity measurements in PEMFC gas diffusion layers and micro porous layers. *J. Power Sources* **206**, 153–160 (2012).
25. Mangal, P. *et al.* Experimental study of mass transport in PEMFCs: Through plane permeability and molecular diffusivity in GDLs. *Electrochim. Acta* **167**, 160–171 (2015).
26. Cekmer, O., LaManna, J. M. & Mench, M. M. Alternative analytical analysis for improved Loschmidt diffusion cell. *Int. J. Heat Mass Transf.* **65**, 883–892 (2013).
27. Yu, Z. & Carter, R. N. Measurement of effective oxygen diffusivity in electrodes for proton exchange membrane fuel cells. *J. Power Sources* **195**, 1079–1084 (2010).
28. Hwang, G. S. & Weber, A. Z. Effective-Diffusivity Measurement of Partially-Saturated Fuel-Cell Gas-Diffusion Layers. *J. Electrochem. Soc.* **159**, F683–F692 (2012).

29. Greszler, T. A., Caulk, D. & Sinha, P. The Impact of Platinum Loading on Oxygen Transport Resistance. *J. Electrochem. Soc.* **159**, F831–F840 (2012).
30. Newman, J. & Thomas-Alyea, K. E. *Electrochemical Systems*. (Wiley, 2004).
31. Wilson, M. S., Valerio, J. A. & Gottesfeld, S. Low platinum loading electrodes for polymer electrolyte fuel cells fabricated using thermoplastic ionomers. *Electrochim. Acta* **40**, 355–363 (1995).
32. Prater, K. The renaissance of the solid polymer fuel cell. *J. Power Sources* **29**, 239–250 (1990).
33. Ralph, T. R. *et al.* Low cost electrodes for proton exchange membrane fuel cells - Performance in single cells and Ballard stacks. *J. Electrochem. Soc.* **144**, 3845–3857 (1997).
34. Ralph, B. T. R. Proton Exchange Membrane Fuel Cells. *Platin. Met. Rev.* **41**, 102–113 (1997).
35. Chen, Z., Waje, M., Li, W. & Yan, Y. Supportless Pt and PtPd nanotubes as electrocatalysts for oxygen-reduction reactions. *Angew. Chemie - Int. Ed.* **46**, 4060–4063 (2007).
36. García-Salaberri, P. A., Hwang, G., Vera, M., Weber, A. Z. & Gostick, J. T. Effective diffusivity in partially-saturated carbon-fiber gas diffusion layers: Effect of through-plane saturation distribution. *Int. J. Heat Mass Transf.* **86**, 319–333 (2015).
37. Owejan, J. P., Trabold, T. A. & Mench, M. M. Oxygen transport resistance correlated to liquid water saturation in the gas diffusion layer of PEM fuel cells. *Int. J. Heat Mass Transf.* **71**, 585–592 (2014).
38. Sinha, P. K., Halleck, P. & Wang, C.-Y. Quantification of Liquid Water Saturation in a PEM Fuel Cell Diffusion Medium Using X-ray Microtomography. *Electrochem. Solid-State Lett.* **9**, A344 (2006).
39. Yin, X. *et al.* Effects of MEA Fabrication and Ionomer Composition on Fuel Cell Performance of

- PGM-free ORR Catalyst. *Trans. E C S Soc. Electrochem.* **77**, 1273–1281 (2017).
40. Zhang, G., Chenitz, R., Lefèvre, M., Sun, S. & Dodelet, J. P. Is iron involved in the lack of stability of Fe/N/C electrocatalysts used to reduce oxygen at the cathode of PEM fuel cells? *Nano Energy* **29**, 111–125 (2016).
 41. Poling, B. E., Prausnitz, J. M. & O'Connell, J. P. *The properties of gases & liquids*. **1**, (McGraw-Hill, 2001).
 42. Kocha, S. S., Vielstich, W., Yokokawa, H. & Gasteiger, H. *Handbook of Fuel Cells: Fuel Cell Technology and Applications Volumes 3 & 4*. (John Wiley & Sons, Ltd, 2010).
 43. Kusoglu, A. & Weber, A. Z. New Insights into Perfluorinated Sulfonic-Acid Ionomers. *Chem. Rev.* **117**, 987–1104 (2017).
 44. Leonard, N. D. *et al.* Modeling of Low-Temperature Fuel Cell Electrodes Using Non-Precious Metal Catalysts. *J. Electrochem. Soc.* **162**, F1253–F1261 (2015).
 45. Serov, A. *et al.* Highly stable precious metal-free cathode catalyst for fuel cell application. *J. Power Sources* **327**, 557–564 (2016).
 46. Cunningham, R. *Diffusion in Gases and Porous Media*. (Springer US, 1980).
 47. Ichikawa, Y. & Selvadurai, A. P. S. Transport phenomena in porous media aspects of micro/macro behaviour /. (2012).
 48. Darling, R. M. A Hierarchical Model for Oxygen Transport in Agglomerates in the Cathode Catalyst Layer of a Polymer-Electrolyte Fuel Cell. **165**, (2018).
 49. Soboleva, T. *et al.* On the micro-, meso-, and macroporous structures of polymer electrolyte membrane fuel cell catalyst layers. *ACS Appl. Mater. Interfaces* (2010). doi:10.1021/am900600y

50. Mench, M. M. *Fuel Cell Engines*. *Fuel Cell Engines* (John Wiley and Sons, 2008).
doi:10.1002/9780470209769
51. Kusoglu, A. *et al.* Impact of substrate and processing on confinement of nafion thin films. *Adv. Funct. Mater.* **24**, 4763–4774 (2014).
52. Chapman, S. & Cowling, T. G. *The Mathematical Theory of Non-Uniform Gases. The Mathematical Theory of Non-Uniform Gases* (Cambridge University Press, 1995). doi:10.1119/1.1942035
53. Komini Babu, S., Chung, H. T., Zelenay, P. & Litster, S. Resolving Electrode Morphology's Impact on Platinum Group Metal-Free Cathode Performance Using Nano-CT of 3D Hierarchical Pore and Ionomer Distribution. *ACS Appl. Mater. Interfaces* **8**, 32764–32777 (2016).
54. Kongkanand, A. & Mathias, M. F. The Priority and Challenge of High-Power Performance of Low-Platinum Proton-Exchange Membrane Fuel Cells. *J. Phys. Chem. Lett.* **7**, 1127–1137 (2016).
55. Normile, S. J. *et al.* Direct observations of liquid water formation at nano- and micro-scale in platinum group metal-free electrodes by operando X-ray computed tomography. *Mater. Today Energy* **9**, 187–197 (2018).
56. Liu, J. *et al.* Understanding the Role of Interfaces for Water Management in Platinum Group Metal-Free Electrodes in Polymer Electrolyte Fuel Cells. *ACS Appl. Energy Mater.* **2**, 3542–3553 (2019).
57. Serov, A. *et al.* Nano-structured platinum group metal-free catalysts and their integration in fuel cell electrode architectures. *Appl. Catal. B Environ.* **237**, 1139–1147 (2018).

